

Photonic spin Hall effect in \mathcal{PT} -symmetric non-Hermitian cavity magnomechanics

Shah Fahad,¹ Muzamil Shah,² and Gao Xianlong^{1,*}

¹*Department of Physics, Zhejiang Normal University, Jinhua, Zhejiang 321004, China*

²*Department of Physics, Quaid-I-Azam University Islamabad, 45320, Pakistan*

(Dated: November 18, 2025)

Non-Hermitian cavity magnomechanics, which incorporates the magnon-photon and magnon-phonon interactions simultaneously, enables rich physical phenomena, including exceptional-point-enhanced sensing, and offers pathways toward topological transitions and nonreciprocal quantum transformation. These interactions exert a pivotal influence on the optical response of a weak probe field and pave the way for novel applications in quantum technologies. In this work, we consider a yttrium-iron-garnet (YIG) sphere coupled to a microwave cavity. The magnon mode of the YIG sphere is directly excited through microwave field coupling, whereas the cavity mode is probed via a weak-field interrogation scheme. The direct interaction of a traveling field with the magnon mode induces gain in the system, thereby establishing non-Hermitian dynamics. The parity-time (\mathcal{PT})-symmetric behavior of a hybrid non-Hermitian cavity magnomechanical system is designed and investigated. Eigenvalue spectrum analysis demonstrates that a third-order exceptional point (EP_3) emerges under tunable effective magnon-photon coupling when the traveling field is oriented at an angle of $\pi/2$ relative to the cavity's x -axis. The photonic spin Hall effect (PSHE) in a reflected probe field is subsequently examined in such a system. Under balanced gain and loss conditions and in the presence of effective magnon-phonon coupling, tunable effective magnon-photon coupling enables coherent control of the PSHE across the broken \mathcal{PT} -symmetric phase, at the EP_3 , and in the \mathcal{PT} -symmetric phase. Investigation reveals that the PSHE can be significantly enhanced or suppressed via effective magnon-photon coupling. The influence of intracavity length on the PSHE is further explored, providing an additional parameter for fine-tuning the transverse shift. These findings establish a direct correspondence between the PSHE and the underlying non-Hermitian eigenvalue spectrum. They further demonstrate that non-Hermitian cavity magnomechanical platforms provide a pathway to tunable photonic functionalities, with immediate prospects for quantum switching and precision sensing.

I. INTRODUCTION

Magnons, the collective spin excitations in magnetic materials [1], have attracted increasing attention as a platform for examining macroscopic quantum phenomena [2–4]. In particular, the cavity magnomechanics system combines magnons, photons, and phonons into a single physical platform, bridging research fields that span quantum information, cavity quantum electrodynamics, magnonics, and quantum optics [5]. This unified framework enables precise characterization of both semi-classical and quantum behaviors, leading to such notable effects as magnon bistability [6, 7], cavity-magnon polaritons [8, 9], high-order sideband generation [10], and the creation of entanglement and squeezed states [11–14]. Beyond these, cavity magnomechanics offers routes to controllable magnonic switching [15], magnon dark modes [16], and exotic non-Hermitian effects [17].

Through the coherent coupling of magnons, phonons, and cavity microwave photons, the microwave response of such systems features magnon-induced absorption and magnomechanically induced transparency [18–23]. These phenomena can be understood via interference mechanisms analogous to those in cavity optomechanics, highlighting the interplay of constructive and destructive

pathways within the system [24–26]. Additionally, cavity magnomechanics has enabled demonstrations of tunable slow and fast light [4, 18, 27] and opened new avenues for combining parity-time (\mathcal{PT})-symmetric paradigms with higher-order sideband control [28].

Unavoidable coupling to the environment in realistic systems induces decoherence [29] and is effectively captured by a non-Hermitian Hamiltonian $H \neq H^\dagger$ [30, 31]. For pseudo-Hermitian Hamiltonians—those satisfying $UHU^{-1} = H^\dagger$ with a linear Hermitian operator U [32, 33]—eigenvalues are either real or occur in complex-conjugate pairs. A prominent subclass is provided by \mathcal{PT} -symmetric Hamiltonians, defined by $[H, \mathcal{PT}] = 0$ [34–36], which embody a characteristic balance of gain and loss. Varying a single control parameter generically drives a \mathcal{PT} -symmetric Hamiltonian through a second-order exceptional point (EP_2), where two eigenvalues and their eigenvectors coalesce, marking the transition from the \mathcal{PT} -symmetric phase (real spectrum) to the \mathcal{PT} -broken phase (complex-conjugate spectrum) [37–39]. EP_2 physics has been extensively explored across platforms including cavity optomechanics [38, 40, 41], waveguides [42], microcavities [43], cavity magnonics [17, 44], and cavity magnomechanics [22]. Beyond EP_2 , non-Hermitian systems can host higher-order exceptional points, at which more than two eigenmodes coalesce [35, 45–48]. Such higher-order singularities exhibit stronger non-Hermitian degeneracies than EP_2 s and enable enhanced sensing [49, 50], richer topological re-

* gaoxl@zjnu.edu.cn

sponses [51, 52], and pronounced spontaneous-emission enhancement [53].

Beyond these explorations, notable applications arise in controlling the transmission of output microwave fields via \mathcal{PT} -symmetric interactions [54, 55]. Underlying many of these phenomena is the concept of magnomechanically induced transparency [20, 56], whereby strong magnon-photon interaction creates a transparent window in the absorption spectrum. Furthermore, the presence of magnon-phonon coupling can engineer multiple transmission windows by suitably adjusting the phase and amplitude of an external magnetic field [21]. Intriguingly, the resulting tunable optical response, along with the attendant group delay control, has been systematically investigated [57], underscoring how fundamental non-Hermitian principles open possibilities for applications in quantum metrology and device engineering.

In this work, we investigate the photonic spin Hall effect (PSHE) as a key aspect of the optical response in a non-Hermitian cavity magnomechanical system. This hybrid platform offers new insights into spin-dependent light-matter interactions and potential control mechanisms for spin-polarized photonic transport.

The PSHE manifests as a spin-dependent spatial separation of photons via spin-orbit coupling [58, 59], inducing a transverse shift in the incident plane for linearly polarized beams composed of right- and left-circular polarization components. This phenomenon constitutes a photonic analog of the electronic spin Hall effect, where refractive index gradients and photon spin mirror the roles of electric potentials and electron spin [60, 61]. Historically attributed to the Imbert-Fedorov displacement [62, 63], the transverse shift has been extensively studied in diverse systems including metamaterials [64], topological insulators [65], graphene heterostructures [66–68], 2D quantum materials [69, 70], plasmonic resonators [71–73], gravitational fields [74], and semiconductors [75].

While the PSHE has been examined in conventional optical and cavity magnomechanical settings [76, 77], its behavior in \mathcal{PT} -symmetric non-Hermitian cavity magnomechanical systems—across the unbroken and broken \mathcal{PT} phases and at the third-order exceptional point EP₃—has not been systematically characterized. Here we address this gap by analyzing a hybrid three-mode platform with magnon-photon and magnon-phonon couplings. We show that, under experimentally feasible parameters, these interactions control spin-dependent transverse shifts: the PSHE exhibits phase-selective responses and pronounced features at EP₃, with its magnitude enhanced or suppressed depending on the underlying non-Hermitian eigenvalue structure. Our results elucidate how \mathcal{PT} symmetry and higher-order exceptional points govern the PSHE in cavity magnomechanics, providing routes to tunable photonic functionalities in engineered non-Hermitian systems.

In this paper, we investigate a non-Hermitian cavity magnomechanical system across broken- \mathcal{PT} , EP₃, and

\mathcal{PT} -symmetric phases. The system comprises a microwave cavity with two fixed mirrors and an embedded yttrium-iron-garnet (YIG) sphere. A uniform B_z -field along the z -direction induces magnon modes in the YIG sphere, coupled to cavity photons via magnetic dipole interaction. Magnetostrictive forces link magnons to phonons via lattice deformation. Non-Hermiticity is engineered through a traveling field driving the magnon mode, introducing gain. At gain-loss balance, we demonstrate a third-order EP₃ by tuning the effective magnon-photon coupling and traveling-field incidence angle. Using the transfer matrix method, we analyze PSHE in reflected probe fields, demonstrating control across all \mathcal{PT} phases. Transverse shifts derived from Fresnel coefficients reveal enhanced PSHE in the \mathcal{PT} -symmetric phase relative to the broken phase, while EP₃ exhibits suppression—consistent with PSHE control via exceptional points [78]. PSHE modulation via intracavity length variation is also demonstrated. These results establish a dynamic control mechanism for spin-dependent photonic transport in non-Hermitian platforms.

The rest of the manuscript is structured as follows: Section II details the physical system and Hamiltonian, Sec. III presents results and discussion, and Sec. V concludes.

II. SYSTEM HAMILTONIAN

We consider a non-Hermitian cavity magnomechanical platform comprising a single-mode microwave cavity \hat{a} (resonance frequency ω_a) and a single-crystal YIG sphere (Fig. 1). The YIG sphere is positioned at the magnetic-field antinode of the cavity mode along the x -axis. The cavity is implemented as a three-layer structure formed by two nonmagnetic mirrors M_1 and M_2 separated by a fixed distance d_2 ; M_2 is perfectly reflecting, whereas M_1 is partially reflecting. Both mirrors have thickness d_1 and permittivities ϵ_1 and ϵ_3 , and the intracavity medium has effective permittivity ϵ_2 , in direct analogy with cavity optomechanical [79] and atomic systems [80]. A uniform z -axis bias field B_z excites a magnon mode \hat{m} (resonance frequency ω_m) in the YIG sphere, which couples to the cavity photons \hat{a} via the magnetic-dipole interaction. Owing to its material quality and geometry, the YIG sphere also functions as a high- Q mechanical resonator \hat{b} (frequency ω_b). Magnetization dynamics associated with \hat{m} drive lattice deformation via magnetostriction, thereby mediating a magnon-phonon coupling through the magnetostrictive force. The resulting hybrid three-mode system supports photon-magnon and magnon-phonon interactions and provides a versatile setting for exploring non-Hermitian cavity magnomechanical phenomena.

The system Hamiltonian is given by

$$\hat{\mathcal{H}} = \hat{\mathcal{H}}_0 + \hat{\mathcal{H}}_c + \hat{\mathcal{H}}_d + \hat{\mathcal{H}}_p + \hat{\mathcal{H}}_{non}, \quad (1)$$

where $\hat{\mathcal{H}}_0 = \hbar\omega_a \hat{a}^\dagger \hat{a} + \hbar\omega_m \hat{m}^\dagger \hat{m} + \hbar\omega_b \hat{b}^\dagger \hat{b}$ describes uncoupled mode energies, $\hat{\mathcal{H}}_c = \hbar g_{ma} (\hat{a} + \hat{a}^\dagger)(\hat{m} +$

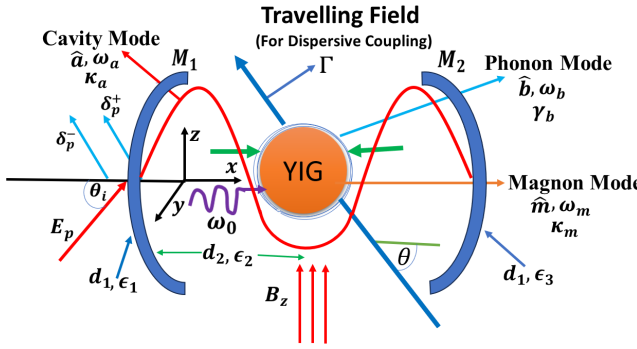


FIG. 1. Schematic illustration of a non-Hermitian cavity magnomechanical system with an embedded YIG sphere. A microwave cavity (photon mode \hat{a} , resonance frequency ω_a , dissipation κ_a) hosts the sphere under z -axis bias field B_z (exciting magnon mode \hat{m} , resonance frequency ω_m , gain κ_m). Magnon-photon coupling occurs via magnetic dipole interaction. Magnetostriction excites phonon mode \hat{b} (ω_b , dissipation γ_b), enabling magnon-phonon coupling enhanced by x -axis microwave drive field (ω_0). Orthogonal cavity (B_y), bias (B_z), and drive (B_x) magnetic fields are shown. Non-Hermiticity arises from a traveling field (incident angle θ , coupling Γ). A TM-polarized probe field E_p incident on mirror M_1 at θ_i undergoes spin-dependent splitting; reflected transverse shifts δ_p^\pm for left/right circular components are measured.

\hat{m}^\dagger) + $\hbar g_{mb} \hat{m}^\dagger \hat{m} (\hat{b}^\dagger + \hat{b})$ governs coherent couplings, $\hat{\mathcal{H}}_d = i\hbar\eta(\hat{m}^\dagger e^{-i\omega_0 t} - \text{H.c.})$ drives the magnon mode, $\hat{\mathcal{H}}_p = i\hbar E_p (\hat{a}^\dagger e^{-i\omega_p t} - \text{H.c.})$ couples the probe field, and $\hat{\mathcal{H}}_{\text{non}} = -i\hbar\Gamma e^{i(\omega t + \theta)} (\hat{a} + \hat{a}^\dagger)(\hat{m} + \hat{m}^\dagger)$ introduces non-Hermiticity. Here, $\omega_{a,m,b}$ denote photon, magnon, and phonon frequencies; \hat{a} , \hat{b} , \hat{m} (\hat{a}^\dagger , \hat{b}^\dagger , \hat{m}^\dagger) are annihilation (creation) operators; g_{ma} (g_{mb}) is the magnon-photon (magnon-phonon) coupling. The magnon mode is driven by a microwave field (frequency ω_0 , amplitude $\eta = \sqrt{5N\gamma B_0}/4$, with the total number of spins N , the external magnetic field B_0 , gyromagnetic ratio γ). A weak probe field (frequency ω_p , power P , incident angle θ_i) couples to the cavity via $E_p = \sqrt{2P\kappa_a/\hbar\omega_p}$. The non-Hermitian term $\hat{\mathcal{H}}_{\text{non}}$ arises from a traveling field (coupling $\Gamma = \frac{\omega_a}{d_2} \sqrt{(\hbar/\omega_m m_m)}$ with the magnon mass m_m) [81–83].

Employing the rotating wave approximation [84, 85], which neglects rapidly oscillating terms under weak-coupling conditions, we transition to a rotating frame where the traveling field becomes effectively time-independent. This field couples to the YIG sphere and introduces gain for the magnon mode. Consequently, Eq. (1) reduces to:

$$\begin{aligned} \hat{\mathcal{H}} = & \hbar\Delta_a \hat{a}^\dagger \hat{a} + \hbar\Delta_m \hat{m}^\dagger \hat{m} + \hbar\omega_b \hat{b}^\dagger \hat{b} \\ & + \hbar(g_{ma} - i\Gamma e^{i\theta})(\hat{a} \hat{m}^\dagger + \hat{a}^\dagger \hat{m}) + \hbar g_{mb} \hat{m}^\dagger \hat{m} (\hat{b}^\dagger + \hat{b}) \\ & + i\hbar\eta(\hat{m}^\dagger - \hat{m}) + i\hbar E_p (\hat{a}^\dagger e^{-i\Delta_p t} - \hat{a} e^{i\Delta_p t}). \end{aligned} \quad (2)$$

Here $\Delta_a = \omega_a - \omega_0$, $\Delta_m = \omega_m - \omega_0$, and $\Delta_p = \omega_p - \omega_0$. The dynamics follow from the Heisenberg-Langevin

equations for operators $\hat{O} \in \hat{a}, \hat{m}, \hat{b}$:

$$\frac{d\hat{O}}{dt} = \frac{i}{\hbar} [\hat{\mathcal{H}}, \hat{O}] - \zeta \hat{O}, \quad (3)$$

where ζ denotes the decay ($\zeta > 0$) or gain ($\zeta < 0$) rate, and $[\hat{O}, \hat{O}^\dagger] = 1$ for $\hat{O} \in \hat{a}, \hat{m}, \hat{b}$. Neglecting quantum and thermal noise [86], we obtain:

$$\begin{aligned} \dot{\hat{a}} &= -(i\Delta_a + \kappa_a)\hat{a} - (ig_{ma} + \Gamma e^{i\theta})\hat{m} + E_p e^{-i\Delta_p t}, \\ \dot{\hat{m}} &= -(i\Delta_m - \kappa_m)\hat{m} - (ig_{ma} + \Gamma e^{i\theta})\hat{a} - ig_{mb}\hat{m}(\hat{b}^\dagger + \hat{b}) + \eta, \\ \dot{\hat{b}} &= -(i\omega_b + \gamma_b)\hat{b} - ig_{mb}\hat{m}^\dagger \hat{m}. \end{aligned} \quad (4)$$

Here κ_a (γ_b) is the photon (phonon) dissipation rate, and κ_m the magnon gain. Replacing operators with expectations $O(t) \equiv \langle \hat{O}(t) \rangle$ ($O = a, m, b$) [87] yields:

$$\begin{aligned} \dot{a} &= -(i\Delta_a + \kappa_a)a - (ig_{ma} + \Gamma e^{i\theta})m + E_p e^{-i\Delta_p t}, \\ \dot{m} &= -(i\Delta_m - \kappa_m)m - (ig_{ma} + \Gamma e^{i\theta})a - ig_{mb}m(b^* + b) + \eta, \\ \dot{b} &= -(i\omega_b + \gamma_b)b - ig_{mb}m^* m. \end{aligned} \quad (5)$$

Steady-state solutions (O_s) satisfy:

$$\begin{aligned} a_s &= \frac{-(ig_{ma} + \Gamma e^{i\theta})m_s}{(i\Delta_a + \kappa_a)}, \\ m_s &= \frac{-(ig_{ma} + \Gamma e^{i\theta})a_s + \eta}{(i\Delta_s - \kappa_m)}, \\ b_s &= \frac{-ig_{mb}|m_s|^2}{(i\omega_b + \gamma_b)}, \end{aligned} \quad (6)$$

where $\Delta_s = \Delta_m + g_{mb}(b_s^* + b_s)$ is the effective magnon-phonon detuning. Linearizing via $O = O_s + \delta O$ and retaining first-order terms gives:

$$\begin{aligned} \dot{\delta a} &= -(i\Delta_a + \kappa_a)\delta a - (ig_{ma} + \Gamma e^{i\theta})\delta m + E_p e^{-i\Delta_p t}, \\ \dot{\delta m} &= -(i\Delta_s - \kappa_m)\delta m - (ig_{ma} + \Gamma e^{i\theta})\delta a - ig_{mb}m_s\delta b, \\ \dot{\delta b} &= -(i\omega_b + \gamma_b)\delta b - ig_{mb}m_s^*\delta m. \end{aligned} \quad (7)$$

A. Effective Hamiltonian and \mathcal{PT} -symmetry

The Heisenberg-Langevin equations in Eq. (7) can be expressed in matrix form as:

$$\dot{\mathbf{O}} = -iH_{\text{eff}} \mathbf{O}, \quad (8)$$

where $\mathbf{O} = (\delta a, \delta m, \delta b)^\top$ is the column vector, and H_{eff} represents the effective non-Hermitian Hamiltonian of the hybrid system,

$$H_{\text{eff}} = \begin{pmatrix} \Delta_a - i\kappa_a & g_{ma} - i\Gamma e^{i\theta} & 0 \\ g_{ma} - i\Gamma e^{i\theta} & \Delta_s + i\kappa_m & G_b \\ 0 & G_b^* & \omega_b - i\gamma_b \end{pmatrix}. \quad (9)$$

Here, $G_b = g_{mb}m_s$ is the effective magnomechanical (magnon-phonon) coupling coefficient. This hybrid three-mode system with magnon-photon and

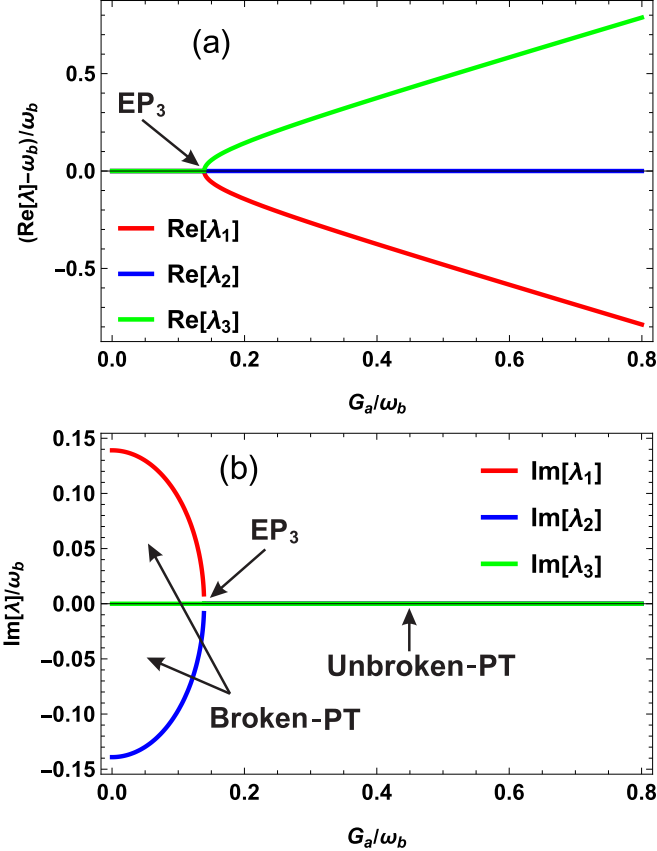


FIG. 2. Eigenvalues of H_{eff} [Eq. (9)] versus normalized effective magnon-photon coupling G_a/ω_b . (a) Real part: $(\text{Re}[\lambda] - \omega_b)/\omega_b$; (b) imaginary part: $\text{Im}[\lambda]/\omega_b$. Parameters: $\kappa_a/2\pi = 2.1$ MHz, $\gamma_b/2\pi = 150$ Hz, $\kappa_m = \kappa_a + \gamma_b$, $\omega_b/2\pi = 15.101$ MHz, $\Delta_s/2\pi = \Delta_a/2\pi = 15.10$ MHz, and $G_b/2\pi = 0.001$ MHz.

magnon–phonon couplings yields three eigenvalues. The eigenvalues λ are determined by:

$$\lambda^3 + r\lambda^2 + s\lambda + t = 0, \quad (10)$$

where $r = -[\Delta_a - i\kappa_a + \Delta_s + i\kappa_m + \omega_b - i\gamma_b]$, $s = (\Delta_a - i\kappa_a)(\Delta_s + i\kappa_m + \omega_b - i\gamma_b) + (\Delta_s + i\kappa_m)(\omega_b - i\gamma_b) - |G_b|^2 - (g_{ma} - i\Gamma e^{i\theta})^2$, $t = -(\Delta_a - i\kappa_a)(\Delta_s + i\kappa_m)(\omega_b - i\gamma_b) + |G_b|^2(\Delta_a - i\kappa_a) + (\omega_b - i\gamma_b)(g_{ma} - i\Gamma e^{i\theta})^2$. The magnon mode is assumed to be driven by a microwave field in the red-sideband regime ($\Delta_a = \Delta_s \approx \omega_b$) [86, 88]. We establish pseudo-Hermiticity conditions for the effective Hamiltonian H_{eff} [Eq. (9)]. Following Refs. [35, 36], H_{eff} is pseudo-Hermitian if: (i) all eigenvalues are real, or (ii) one is real and the others form a complex-conjugate pair. At $\theta = \pi/2$, the spectrum satisfies $\det(H_{\text{eff}} - \lambda I) = \det(H_{\text{eff}}^* - \lambda I) = 0$, where I is the identity matrix. The parameters of the system should satisfy the following constraints:

$$\begin{aligned} \kappa_a + \gamma_b - \kappa_m &= 0, \\ \kappa_a \kappa_m \gamma_b - \kappa_a |G_b|^2 - \gamma_b (g_{ma} - i\Gamma e^{i\theta})^2 &= 0. \end{aligned} \quad (11)$$

According to Eq. (11), the effective Hamiltonian H_{eff} is

pseudo-Hermitian. Under the balanced gain-loss condition ($\kappa_m = \kappa_a + \gamma_b$) and a traveling-field phase $\theta = \pi/2$, H_{eff} exhibits a \mathcal{PT} -symmetric eigenvalue spectrum for $0 < G_b \lesssim 2\pi \times 0.01$ MHz, a parameter window contained within the broader pseudo-Hermitian regime [34–36]. Henceforth, we classify and discuss the system’s behavior in terms of the corresponding \mathcal{PT} phases.

Figure 2 (a) and (b) display the eigenvalue spectrum of the non-Hermitian cavity magnomechanical system versus normalized effective magnon-photon coupling G_a/ω_b , where $G_a = (g_{ma} - i\Gamma e^{i\theta})$ at $\theta = \pi/2$. Under balanced gain-loss ($\kappa_m = \kappa_a + \gamma_b$), the broken \mathcal{PT} -symmetric phase ($G_a/\omega_b < 0.139$) exhibits complex eigenvalues with nonzero real and imaginary components. At $G_a/\omega_b = 0.139$, eigenvalue coalescence forms a third-order exceptional point (EP₃). For $G_a/\omega_b > 0.139$, the unbroken \mathcal{PT} -symmetric phase features three real eigenvalues.

To assess the impact of the effective magnon-phonon coupling strength G_b on the spectrum, we analyze two representative cases: $G_b = 0$ and $G_b = 2\pi \times 0.05$ MHz. For $G_b = 0$, Eq. (10) reduces to $(\lambda - (\omega_b - i\gamma_b))(\lambda^2 + A\lambda + B) = 0$, where $A = -(2\omega_b + i\gamma_b)$ and $B = \omega_b^2 + i\omega_b\gamma_b + \kappa_a^2 + \kappa_a\gamma_b - G_a^2$. In this uncoupled case, the mechanical mode eigenvalue $\lambda_1 = \omega_b - i\gamma_b$ remains distinct from the magnon-photon subsystem eigenvalues $\lambda_{2,3}$, and coalescence occurs only within the magnon–photon subsystem. The corresponding eigenvalues of H_{eff} as functions of G_a/ω_b are shown in Fig. 3. For $G_b = 0$, an EP₂ is clearly visible [panel (a)]. Although the Hamiltonian remains formally 3×3 due to the phonon term ($\omega_b - i\gamma_b$), the phonon mode is decoupled from the magnon-photon subsystem. The characteristic polynomial is therefore cubic, but a genuine EP₃ cannot arise because the three modes are not mutually coupled. The apparent triple root in [panel (a)] occurs when $\omega_b - i\gamma_b$ coincides with a doubly degenerate eigenvalue of the magnon-photon sector; this is an algebraic (accidental) degeneracy without coalescence of three eigenvectors, and thus not a robust EP₃. In this limit, the system effectively reduces to a non-Hermitian magnonic model rather than a magnomechanical one. For $G_b = 2\pi \times 0.05$ MHz, the EP₃ is lifted [panel (b)], highlighting G_b as a key control parameter of the spectral structure. In the experimentally relevant regime where G_b is on the order of kHz—much smaller than the remaining (MHz-scale) parameters [Eq. (10)]—the spectrum remains \mathcal{PT} -symmetric for $0 < G_b \lesssim 2\pi \times 0.01$ MHz, and the EP₃ persists [Fig. 2]. Increasing G_b beyond this window lifts the triple degeneracy and eliminates the EP₃ [panel (b)].

B. Optical Susceptibility

To find the optical susceptibility of the coupled system, we solve Eq. (7) by introducing the slowly varying operator for the linear terms of the fluctuation as $\delta a \rightarrow \delta a e^{-i\Delta_a t}$, $\delta m \rightarrow \delta m e^{-i\Delta_s t}$, and $\delta b \rightarrow \delta b e^{-i\omega_b t}$.

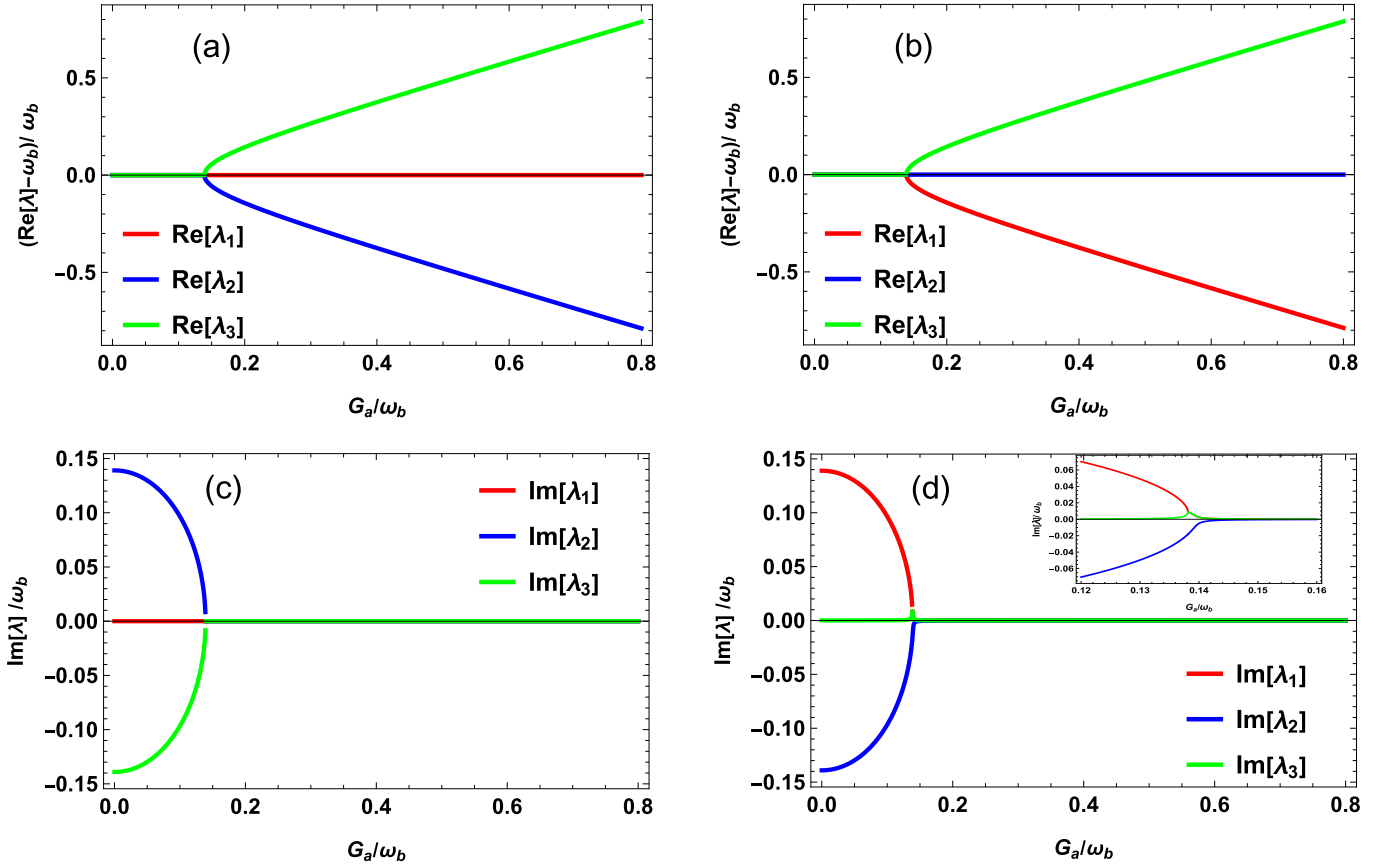


FIG. 3. Eigenvalues of H_{eff} [Eq. (9)] as a function of G_a/ω_b . (a,b) Real parts: $(\text{Re}[\lambda] - \omega_b)/\omega_b$; (c,d) Imaginary parts: $\text{Im}[\lambda]/\omega_b$. Columns correspond to effective magnon–phonon coupling strengths $G_b = 0$ and $G_b/2\pi = 0.05$ MHz, respectively. The inset in Fig. 3(d) provides a magnified view of $\text{Im}[\lambda]/\omega_b$ as a function of G_a/ω_b . Fixed parameters: $\kappa_a/2\pi = 2.1$ MHz, $\gamma_b/2\pi = 150$ Hz, $\kappa_m = \kappa_a + \gamma_b$, $\omega_b/2\pi = 15.101$ MHz, $\Delta_s/2\pi = \Delta_a/2\pi = 15.10$ MHz, and at $G_b = 0$, $\Delta_m/2\pi = \Delta_a/2\pi = 15.10$ MHz.

Then Eq. (7) can be written as

$$\begin{aligned} \delta\dot{a} &= -\kappa_a\delta a - (ig_{ma} + \Gamma e^{i\theta})\delta m + E_p e^{-ixt}, \\ \delta\dot{m} &= +\kappa_m\delta m - (ig_{ma} + \Gamma e^{i\theta})\delta a - ig_{mb}m_s\delta b, \\ \delta\dot{b} &= -\gamma_b\delta b - ig_{mb}m_s^*\delta m, \end{aligned} \quad (12)$$

where $x = \Delta_p - \omega_b$ is the effective detuning. To solve Eq. (12), we apply the ansatz $\delta A = \delta A_1 e^{-ixt} + \delta A_2 e^{ixt}$ with $A = (a, m, b)$. Therefore, we obtain the first-order sideband amplitude δa_1 of the non-Hermitian cavity magnomechanical system for a weak probe field:

$$\delta a_1 = \frac{E_p}{(\kappa_a - ix) + \frac{(\gamma_b - ix)(ig_{ma} + \Gamma e^{i\theta})^2}{(\kappa_m + ix)(\gamma_b - ix) - G_b^2}}. \quad (13)$$

In this analysis, the contribution from δa_2 is negligible, as it corresponds to a four-wave mixing process at frequency $\omega_p - 2\omega_0$ induced by the interaction between the weak probe field and the driving field. The output field E_T of the weak probe field defines the optical susceptibility χ through the relation [77, 86, 89, 90]

$$\chi \equiv E_T = \kappa_a \delta a_1 / E_p, \quad (14)$$

where χ is a complex quantity expressed in quadrature components as $\chi = \chi_r + i\chi_i$. These quadratures are measured via homodyne detection [91]. The real part χ_r governs the absorption spectrum, while the imaginary part χ_i determines the dispersion spectrum of the weak probe field.

The PSHE constitutes an optical analog of the electronic SHE [92]. The reflection coefficients for TE polarization (r^s) and TM polarization (r^p) are computed for the cavity using the transfer matrix method. The transfer matrix of the effective three-layer system is given by

$$M_j^{s,p}(\theta_i, \omega_p, d_j) = \begin{pmatrix} \cos[n_j k \cos(\theta_j) d_j] & i\beta_j^{s,p} \sin[n_j k \cos(\theta_j) d_j] / [n_j \cos(\theta_j)] \\ i n_j \cos(\theta_j) \sin[n_j k \cos(\theta_j) d_j] / \beta_j^{s,p} & \cos[n_j k \cos(\theta_j) d_j] \end{pmatrix}. \quad (15)$$

Here, $k = \omega_p/c$ is the vacuum wavenumber of the probe field, where c is the speed of light. The refraction angle θ_j at the j -th interface satisfies Snell's law: $n_i \sin(\theta_i) = n_j \sin(\theta_j)$, where θ_i is the incident angle. For each layer

($j = 1, 2, 3$), n_j and d_j denote the refractive index and thickness, respectively. The polarization-dependent parameter is $\beta_j^s = \epsilon_j$ (TE mode) and $\beta_j^p = \mu_j$ (TM mode). The cavity's total 2×2 transfer matrix is given by

$$X^{s,p}(\theta_i, \omega_p) = M_1^{s,p}(\theta_i, \omega_p, d_1) M_2^{s,p}(\theta_i, \omega_p, d_2) M_1^{s,p}(\theta_i, \omega_p, d_1) = \begin{pmatrix} X_{11}^{s,p} & X_{12}^{s,p} \\ X_{21}^{s,p} & X_{22}^{s,p} \end{pmatrix}, \quad (16)$$

where $M_j^{s,p}(\theta_i, \omega_p, d_j)$ depends on the parameters of the respective layer, and the superscript (s, p) indicates the incident wave polarization. The Fresnel reflection coefficients r^s and r^p are [93]

$$r^{s,p}(\theta_i, \omega_p) = \frac{\cos \theta (X_{22}^{s,p} - X_{11}^{s,p}) - (\cos^2 \theta X_{12}^{s,p} - X_{21}^{s,p})}{\cos \theta (X_{22} + X_{11}) - (\cos^2 \theta X_{12}^{s,p} + X_{21}^{s,p})}. \quad (17)$$

Here, $X_{ij}^{s,p}$ (with $i, j = 1, 2$) denote the matrix elements of $X^{s,p}(\theta_i, \omega_p)$. Equation (17) reveals that the reflection coefficients depend on the cavity permittivity ϵ_2 , tunable via the susceptibility χ through $\epsilon_2 = 1 + \chi$. The spin-dependent transverse shift is consequently derived from the Fresnel reflection coefficients.

We consider a Gaussian-shaped probe field incident on the interface of a cavity magnomechanical system, whose angular spectrum is given by:

$$\tilde{E}_i = \frac{w_0}{\sqrt{2\pi}} \exp \left(-\frac{w_0^2(k_{ix}^2 + k_{iy}^2)}{4} \right), \quad (18)$$

$$\mathbf{E}_{r\pm}^p(x_r, y_r, z_r) = \frac{(\mathbf{e}_{rx} \pm i\mathbf{e}_{ry})}{\sqrt{\pi}w_0} \frac{z_R}{z_R + iz_r} \exp(ik_r z_r) \exp \left[-\frac{k}{2} \frac{x_r^2 + y_r^2}{z_R + iz_r} \right] \times \left[r^p - \frac{ix}{z_R + iz_r} \frac{\partial r^p}{\partial \theta_i} \pm \frac{y}{z_R + iz_r} (r^p + r^s) \pm \frac{ixy}{(z_R + iz_r)^2} \left(\frac{\partial r^p}{\partial \theta_i} + \frac{\partial r^s}{\partial \theta_i} \right) \right], \quad (20)$$

where (x_r, y_r, z_r) denote the Cartesian coordinates of the reflected beam path, $z_R = kw_0^2/2$ is the Rayleigh length, and \mathbf{e}_{rx} and \mathbf{e}_{ry} are the x - and y -components, respectively, of the reflected electric field's polarization unit vector. The transverse displacements of the reflected weak probe field are then given by

$$\delta_p^\pm = \frac{\int y_r |E_{r\pm}^p(x_r, y_r, z_r)|^2 dx_r dy_r}{\int |E_{r\pm}^p(x_r, y_r, z_r)|^2 dx_r dy_r}. \quad (21)$$

Based on Eqs. (20) and (21), the spin-dependent transverse components of the reflected probe field in the effective three-layer cavity magnomechanical system can be written as [94, 96]

$$\delta_p^\pm = \mp \frac{kw_0^2 \text{Re}[1 + \frac{r^s}{r^p}] \cot \theta_i}{k^2 w_0^2 + |\frac{\partial \ln r^p}{\partial \theta_i}|^2 + |(1 + \frac{r^s}{r^p}) \cot \theta_i|^2}. \quad (22)$$

where w_0 is the beam waist radius, and k_{ix}, k_{iy} denote the incident probe field's wavevector x - and y -components, respectively [78, 94]. Enforcement of boundary conditions [94–96] yields the Fresnel coefficients, from which the reflected angular spectrum is derived,

$$\begin{pmatrix} \tilde{E}_r^p \\ \tilde{E}_r^s \end{pmatrix} = \begin{pmatrix} r^p & \frac{k_{ry} \cot \theta_i (r^p + r^s)}{k} \\ -\frac{k_{ry} \cot \theta_i (r^p + r^s)}{k} & r^s \end{pmatrix} \begin{pmatrix} \tilde{E}_i^p \\ \tilde{E}_i^s \end{pmatrix}, \quad (19)$$

where k_{ry} is the reflected wavevector's y -component. The incident angular spectra for p - and s -polarized probe field components are denoted by \tilde{E}_i^p and \tilde{E}_i^s , respectively. We consider a p -polarized Gaussian probe field. The reflected angular spectrum determines the circular components of the reflected field, \mathbf{E}_{r+}^p and \mathbf{E}_{r-}^p , corresponding to right- (δ_p^+) and left-handed (δ_p^-) circularly polarized states, respectively [94],

III. RESULTS AND DISCUSSION

This section presents the numerical results. The parameters are adopted from a recent experimental study of a hybrid cavity magnomechanical system [97]: mechanical frequency $\omega_b/2\pi = 15.101$ MHz, cavity decay rate $\kappa_a/2\pi = 2.1$ MHz, cavity frequency $\omega_a/2\pi = 1.32$ GHz, mechanical damping rate $\gamma_b/2\pi = 150$ Hz, magnon gain rate $\kappa_m = \kappa_a + \gamma_b$, and effective magnomechanical coupling rate $G_b/2\pi = 0.001$ MHz. The YIG sphere has diameter $D = 250$ μm , spin density $\rho = 4.22 \times 10^{27} \text{ m}^{-3}$, gyromagnetic ratio $\gamma/2\pi = 28$ GHz/T, and is subject to a driving magnetic field $B_0 \leq 0.5$ mT, corresponding to $G_b/2\pi \leq 1.5$ MHz [22]. For the PSHE investigation, the dielectric constants are $\epsilon_0 = 1$, $\epsilon_1 = \epsilon_3 = 2.2$, with layer thicknesses $d_1 = 4$ mm and $d_2 = 45$ mm [21, 97]. The in-

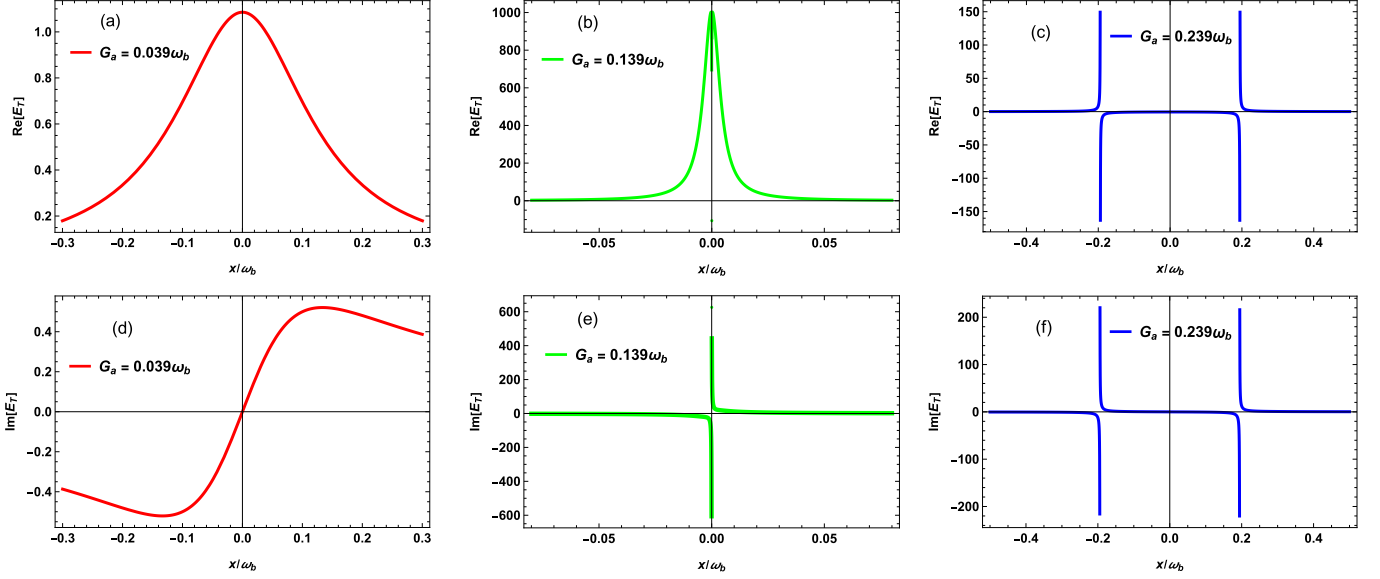


FIG. 4. (a-c) Absorption spectra (real part of the output field E_T) and (d-f) dispersion spectra (imaginary part of E_T) versus normalized effective detuning x/ω_b . Columns correspond to $G_a = 0.039 \omega_b$ (broken \mathcal{PT} -symmetry, red), $0.139 \omega_b$ (third-order exceptional point EP_3 , green), and $0.239 \omega_b$ (\mathcal{PT} -symmetry, blue). Fixed parameters: $\kappa_a/2\pi = 2.1$ MHz, $\gamma_b/2\pi = 150$ Hz, $\kappa_m = \kappa_a + \gamma_b$, $\omega_b/2\pi = 15.101$ MHz, and $G_b/2\pi = 0.001$ MHz.

incident beam is well-collimated with waist $w_0 = 50 \lambda$ [76]. The system exhibits \mathcal{PT} -symmetry solely when the traveling field angle relative to the cavity x -axis is $\pi/2$.

Numerical results for the PSHE are presented in three regimes: (i) broken \mathcal{PT} -symmetry, (ii) EP_3 , and (iii) \mathcal{PT} -symmetric phase, as defined in Sec. II A. Figure 4 shows the probe field's absorption [Re(E_T)] and dispersion [Im(E_T)] spectra versus normalized effective detuning x/ω_b across these regimes. Panel (a) displays the broken- \mathcal{PT} -symmetry absorption spectrum with complex conjugate eigenvalues, exhibiting a Lorentzian peak at resonance ($x = 0$). At the EP_3 [panel (b)], eigenvalue-eigenvector coalescence induces a sharp absorption peak at $x = 0$, signifying enhanced sensitivity to perturbations. The \mathcal{PT} -symmetric phase [panel (c)] reveals symmetric absorption resonances with balanced positive/negative amplitudes about $x = 0$ [98], indicating strong magnon-photon coherence. Panels (d)-(f) present corresponding dispersion spectra. The EP_3 [panel (e)] exhibits a divergence at $x = 0$, corresponding to a rapid probe phase change. The \mathcal{PT} -symmetric regime [panel (f)] displays asymmetric resonances about $x = 0$, characteristic of \mathcal{PT} -symmetric systems [98].

Equation (22) indicates that the spin-dependent transverse shift depends on the Fresnel reflection coefficients $|r^s|$ and $|r^p|$ for TE- and TM-polarized probe fields. We therefore analyze $|r^s|$ and $|r^p|$ versus incident angle θ_i (radians) in the broken \mathcal{PT} -symmetric phase, at the EP_3 , and in the \mathcal{PT} -symmetric phase. Figure 5(a) displays $|r^s|$ and $|r^p|$ at resonance ($x = 0$). At the EP_3 , both coefficients remain constant (≈ 1), indicating near-total reflection due to eigenvalue-eigenvector coalescence that suppresses spin-dependent responses. In broken and \mathcal{PT} -symmetric phases, low coefficients at small θ_i imply in-

creased transmission and reduced reflection. As θ_i increases, $|r^s|$ (dashed curves) rises while $|r^p|$ (solid curves) decreases, vanishing at Brewster angles $\theta_B = 0.538$ rad (\mathcal{PT} -symmetric) and $\theta_B = 0.962$ rad (broken phase). This vanishing reflection, characteristic of TM polarization at Brewster's angle, occurs when reflected and refracted rays become orthogonal. Beyond θ_B , $|r^p|$ increases, restoring TM reflection. These trends, consistent with Refs. [76, 99], enable transverse shift examination through reflection coefficient differences in the present non-Hermitian cavity magnomechanical system in the broken \mathcal{PT} -symmetric phase, EP_3 , and \mathcal{PT} -symmetric phase.

The ratio $|r^s|/|r^p|$ of TE- to TM-polarized reflection coefficients is analyzed next, as Eq. (22) shows the spin-dependent transverse shift depends critically on this ratio. Enhancement occurs when $|r^s|/|r^p| > 1$. Figure 5(b) plots $|r^s|/|r^p|$ versus θ_i at resonance ($x = 0$) for broken \mathcal{PT} -symmetric (red), EP_3 (green), and \mathcal{PT} -symmetric (blue) phases. Near Brewster angles $\theta_B = 0.538$ rad (\mathcal{PT} -symmetric) and $\theta_B = 0.962$ rad (broken phase), the ratio surges due to the contrasting approaches of TE- and TM-polarized components of probe field with the interface at this specific angle in \mathcal{PT} -symmetric and broken- \mathcal{PT} -symmetric phases, respectively. At these angles, $|r^p|$ vanishes [Fig. 5(a), solid curves] from destructive interference at the interface, while $|r^s|$ remains finite (dashed curves). This disparity enhances $|r^s|/|r^p|$ as TM polarization refracts entirely into the second medium while TE reflects. Characterization requires narrow θ_i ranges near θ_B . At the EP_3 , absent phase contrast [Fig. 5(a)] maintains $|r^s|/|r^p| < 1$ [Fig. 5(b)].

The normalized PSHE δ_p^+/λ , arising from the right-circularly polarized component of the reflected probe

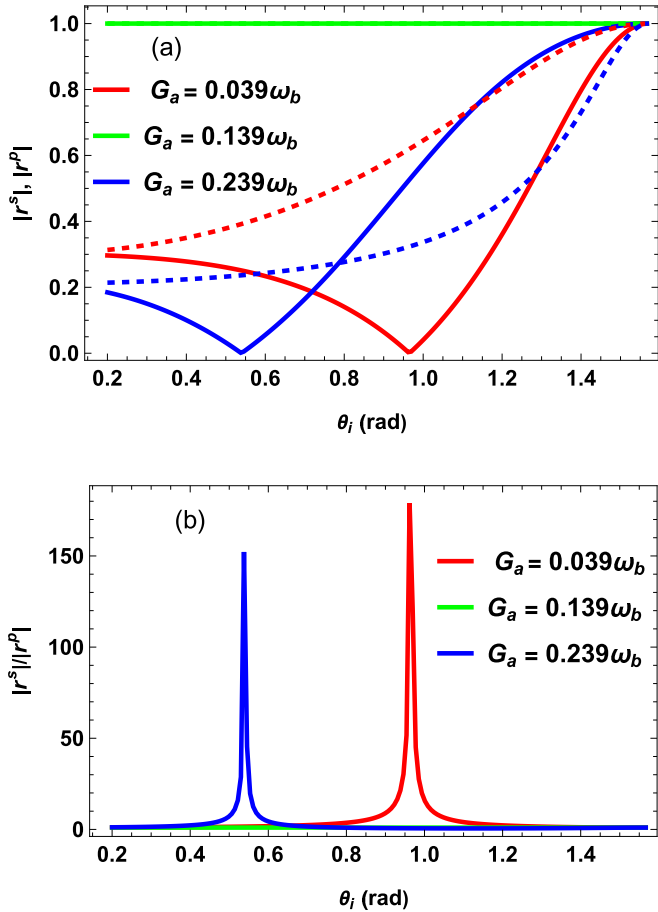


FIG. 5. (a) Absolute values of the reflection coefficients $|r^s|$ (dashed) and $|r^p|$ (solid), and (b) their ratio $|r^s|/|r^p|$ versus incident angle θ_i , at $G_a = 0.039\omega_b$, $0.139\omega_b$, and $0.239\omega_b$, corresponding to the broken \mathcal{PT} -symmetric (red), EP₃ (green), and \mathcal{PT} -symmetric (blue) phases at the resonance condition $x = 0$, respectively. Other parameters are $\kappa_a/2\pi = 2.1$ MHz, $\gamma_b/2\pi = 150$ Hz, $\kappa_m = \kappa_a + \gamma_b$, $\omega_b/2\pi = 15.101$ MHz, $G_b/2\pi = 0.001$ MHz, $\omega_a/2\pi = 1.32$ GHz, $w_0 = 50\lambda$, $d_1 = 4$ mm, $d_2 = 45$ mm, $\epsilon_0 = 1$, and $\epsilon_1 = \epsilon_3 = 2.2$.

field, is analyzed. The left-circularly polarized component δ_p^-/λ exhibits an equal-magnitude shift in the opposite direction due to circular polarization symmetry; thus, δ_p^+/λ fully characterizes the transverse shift. Figure 6 shows δ_p^+/λ versus θ_i for broken \mathcal{PT} -symmetric (red), EP₃ (green), and \mathcal{PT} -symmetric (blue) phases at resonance ($x = 0$). In the \mathcal{PT} -symmetric phase, the shift transitions from negative ($\theta_i < 0.538$ rad) to positive ($\theta_i > 0.538$ rad). Similarly, the broken phase exhibits sign reversal at $\theta_i = 0.962$ rad. This sign inversion stems from a π phase shift in reflection coefficients $|r^s|$ and $|r^p|$. Resonance enhancement ($x = 0$) originates from phase differences between TE/TM Fresnel coefficients, amplifying constructive interference. The \mathcal{PT} -symmetric phase yields larger shifts than the broken phase, reflecting superior spin-state discrimination and coherence preservation in the non-Hermitian cavity magnomechanical system. At the EP₃, eigenvalue-eigenvector coalescence sup-

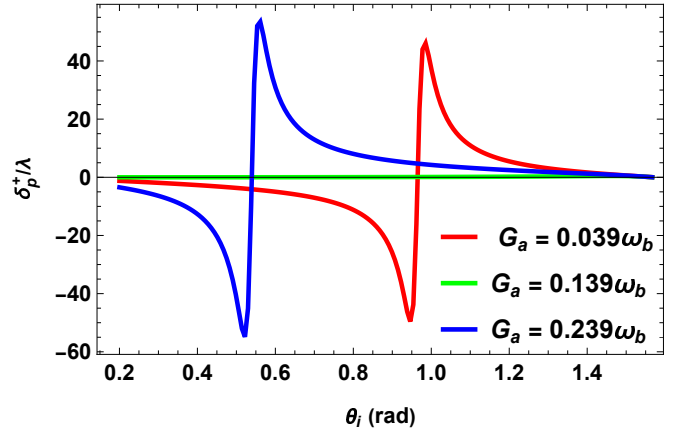


FIG. 6. Normalized PSHE δ_p^+/λ versus incident angle θ_i (rad) at $G_a = 0.039\omega_b$, $0.139\omega_b$, and $0.239\omega_b$, corresponding to the broken \mathcal{PT} -symmetric (red), EP₃ (green), and \mathcal{PT} -symmetric (blue) phases at the resonance condition $x = 0$, respectively. Other parameters are $\kappa_a/2\pi = 2.1$ MHz, $\gamma_b/2\pi = 150$ Hz, $\kappa_m = \kappa_a + \gamma_b$, $\omega_b/2\pi = 15.101$ MHz, $G_b/2\pi = 0.001$ MHz, $\omega_a/2\pi = 1.32$ GHz, $w_0 = 50\lambda$, $d_1 = 4$ mm, $d_2 = 45$ mm, $\epsilon_0 = 1$, and $\epsilon_1 = \epsilon_3 = 2.2$.

presses spin-orbit interaction, inhibiting mode orthogonality and reducing the shift. These results agree with EP-mediated spin Hall control [78]. Such spin-orbit coupling manipulation enables spin-selective photonic devices.

Figure 7 (a) and (b) show the influence of the effective magnon-phonon coupling G_b on the PSHE δ_p^+/λ as a function of the probe field's incident angle θ_i . We compare two illustrative cases: $G_b = 0$ and $G_b = 2\pi \times 0.05$ MHz. For $G_b = 0$, the system exhibits a clear phase transition in the PSHE [Fig. 7(a)], consistent with the \mathcal{PT} -symmetric eigenvalue spectrum [Fig. 3 panel (a)]. In contrast, when $G_b = 2\pi \times 0.05$ MHz, the magnon-phonon interaction not only suppresses the PSHE but also destroys the associated \mathcal{PT} phase transition [Fig. 7(b)]. This suppression is primarily attributed to enhanced absorption at resonance induced by G_b [76]. These findings demonstrate the critical role of G_b in shaping both the \mathcal{PT} -symmetric eigenvalue spectrum and the spin-dependent splitting of the probe field in the PSHE.

The PSHE δ_p^+/λ is examined versus incident angle θ_i and normalized effective detuning x/ω_b across \mathcal{PT} -symmetry phases. Distinct characteristics emerge in broken \mathcal{PT} -symmetric, EP₃, and \mathcal{PT} -symmetric phases. The contour plots of normalized photonic spin Hall shift δ_p^+/λ versus incident angle θ_i and normalized effective detuning x/ω_b show that, the maximum shift transitions from negative ($\theta_i < 0.962$ rad) to positive ($\theta_i > 0.962$ rad) in the broken \mathcal{PT} -symmetric phase [Fig. 8(a)], while suppression characterizes the EP₃ [Fig. 8(b)]. Similarly, the \mathcal{PT} -symmetric phase exhibits sign reversal at $\theta_i = 0.538$ rad [Fig. 8(c)]. This agreement validates the physical interpretation of the PSHE.

The PSHE δ_p^+/λ depends critically on cavity geometry, particularly total thickness $L = 2d_1 + d_2$, ne-

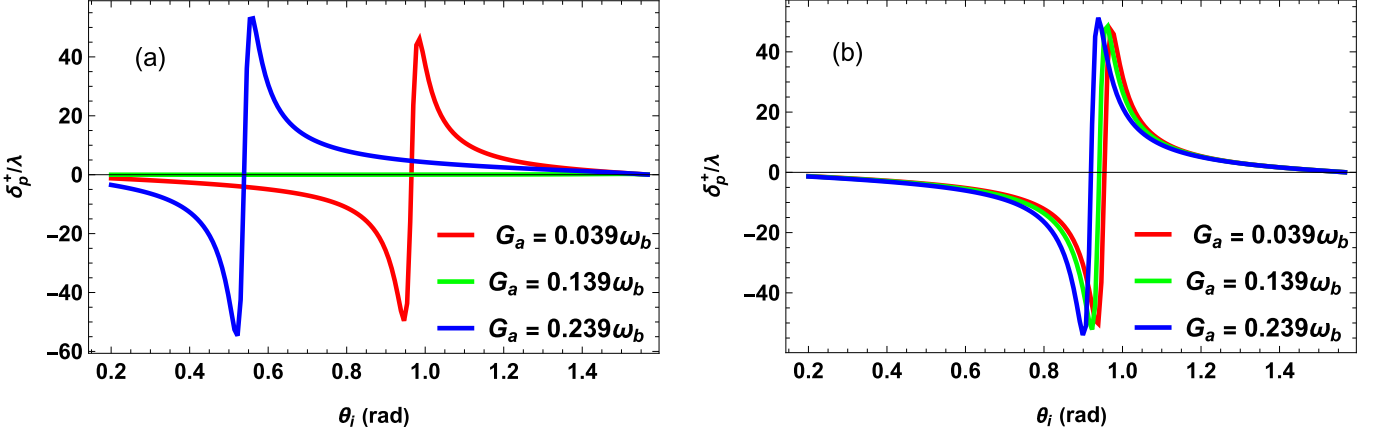


FIG. 7. Normalized PSHE δ_p^+/λ as a function of the incident angle θ_i (rad) at resonance ($x = 0$) for effective magnon-phonon coupling strengths: (a) $G_b = 0$ and (b) $G_b/2\pi = 0.05$ MHz. Fixed parameters: $G_a = 0.039 \omega_b$ (broken \mathcal{PT} -symmetric, red), $G_a = 0.139 \omega_b$ (EP₃, green), $G_a = 0.239 \omega_b$ (\mathcal{PT} -symmetric, blue), $\kappa_a/2\pi = 2.1$ MHz, $\gamma_b/2\pi = 150$ Hz, $\kappa_m = \kappa_a + \gamma_b$, $\omega_b/2\pi = 15.101$ MHz, $\omega_a/2\pi = 1.32$ GHz, $w_0 = 50 \lambda$, $d_1 = 4$ mm, $d_2 = 45$ mm, $\epsilon_0 = 1$, and $\epsilon_1 = \epsilon_3 = 2.2$.

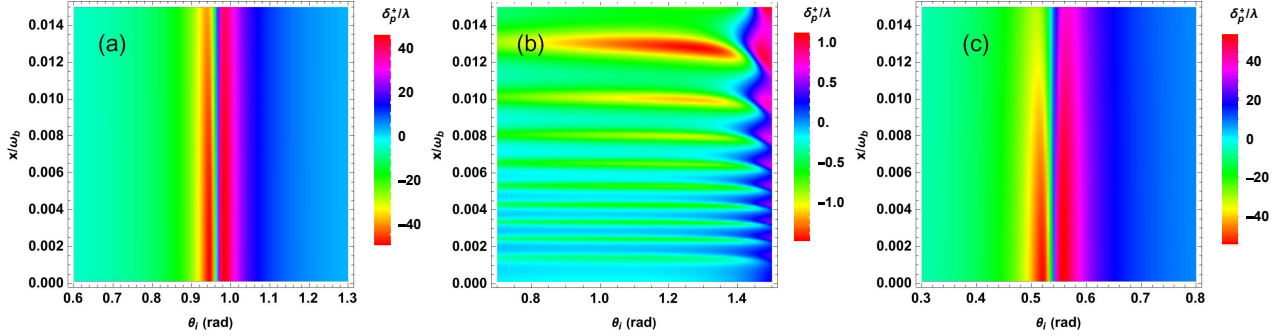


FIG. 8. Contour plots of normalized photonic spin Hall shift δ_p^+/λ versus incident angle θ_i and normalized effective detuning x/ω_b for: (a) broken \mathcal{PT} -symmetric phase ($G_a = 0.039 \omega_b$), (b) EP₃ ($G_a = 0.139 \omega_b$), and (c) \mathcal{PT} -symmetric phase ($G_a = 0.239 \omega_b$). Fixed parameters: $\kappa_a/2\pi = 2.1$ MHz, $\gamma_b/2\pi = 150$ Hz, $\kappa_m = \kappa_a + \gamma_b$, $\omega_b/2\pi = 15.101$ MHz, $G_b/2\pi = 0.001$ MHz, $\omega_a/2\pi = 1.32$ GHz, $w_0 = 50 \lambda$, $d_1 = 4$ mm, $d_2 = 45$ mm, $\epsilon_0 = 1$, and $\epsilon_1 = \epsilon_3 = 2.2$.

cessitating precise dimensional control. Figures 9(a-c) show δ_p^+/λ versus θ_i at resonance ($x = 0$) for intracavity lengths $d_2 = 45$, 55, and 65 mm. In the broken \mathcal{PT} -symmetric phase [Fig. 9(a)], the shift magnitude increases with d_2 while shifting toward smaller θ_i . The EP₃ [Fig. 9(b)] exhibits length-independent suppression. The \mathcal{PT} -symmetric phase [Fig. 9(c)] shows reduced shift magnitudes and shifts toward larger θ_i with increasing d_2 . These opposing trends between symmetry phases arise from modified phase accumulation and interference conditions, demonstrating the critical role of intracavity length in PSHE control.

IV. CONCLUSION

In summary, we have investigated \mathcal{PT} -symmetric dynamics in a hybrid non-Hermitian cavity magnomechanical system with magnon-photon and magnon-phonon interactions. Eigenvalue spectrum analysis reveals that a third-order exceptional point (EP₃) emerges under bal-

anced gain-loss conditions when the traveling field is oriented at $\pi/2$ relative to the cavity's x -axis, delineating three distinct phases: (i) broken \mathcal{PT} -symmetry, (ii) EP₃, and (iii) \mathcal{PT} -symmetric.

The photonic spin Hall effect (PSHE) for a reflected probe field exhibits phase-dependent characteristics. At resonance ($x = 0$), the \mathcal{PT} -symmetric phase yields significantly enhanced transverse shifts compared to the broken phase, demonstrating superior spin-state discrimination. Conversely, eigenvalue-eigenvector coalescence at the EP₃ suppresses spin-orbit interactions, inhibiting the PSHE. Intracavity length modulation provides additional control, inducing opposing trends in shift magnitude and angular dependence between \mathcal{PT} -symmetric and broken phases due to modified interference conditions. These results establish non-Hermitian cavity magnomechanics as a versatile platform for coherent spin-photon control, with promising applications in spin-selective photonic devices, quantum switching, and high-precision microwave sensing.

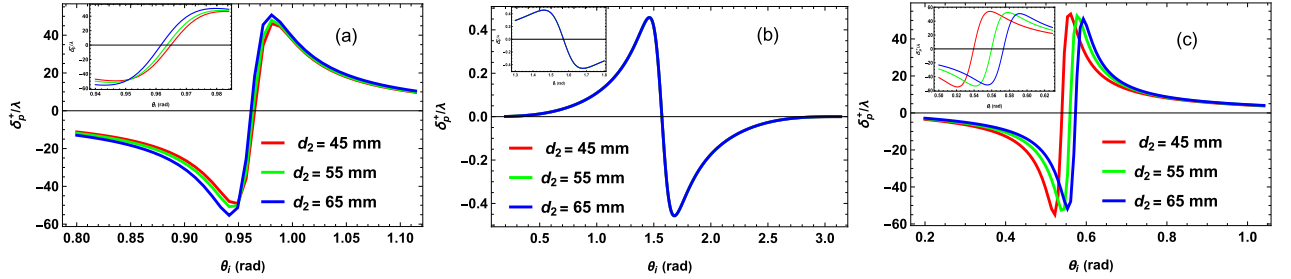


FIG. 9. Normalized photonic spin Hall shift δ_p^+/λ as a function of incident angle θ_i for (a) broken \mathcal{PT} -symmetric phase ($G_a = 0.039 \omega_b$), (b) EP3 ($G_a = 0.139 \omega_b$), and (c) \mathcal{PT} -symmetric phase ($G_a = 0.239 \omega_b$), respectively at three different intracavity medium lengths. Red, green, and blue curves show the PSHE at $d_2 = 45$ mm, 55 mm, and 65 mm, respectively, at the resonance condition $x = 0$. The insets in Figs. 9(a–c) provide magnified views of δ_p^+/λ as a function of θ_i for each phase at different intracavity medium lengths. Other parameters are $\kappa_a/2\pi = 2.1$ MHz, $\gamma_b/2\pi = 150$ Hz, $\kappa_m = \kappa_a + \gamma_b$, $\omega_b/2\pi = 15.101$ MHz, $G_b/2\pi = 0.001$ MHz, $\omega_a/2\pi = 1.32$ GHz, $w_0 = 50 \lambda$, $d_1 = 4$ mm, $\epsilon_0 = 1$, and $\epsilon_1 = \epsilon_3 = 2.2$.

The assumption of magnon gain in our model is well-supported by established experimental techniques. In particular, gain can be realized through parametric parallel pumping, where a microwave field at twice the magnon resonance frequency ($\omega_p \approx 2\omega_m$) is applied to the magnetic medium (YIG sphere). This process parametrically amplifies the magnon population and leads to an effective negative damping (i.e., gain) of the magnon mode [100–102]. In our Hamiltonian, the traveling field term represents this external pump, which can be implemented experimentally using a microwave antenna or waveguide. Recent experiments have shown that such microwave pumping not only generates pump-induced magnon modes but also drives them into strong coupling with other magnetic excitations, a phenomenon that cru-

cially relies on the presence of magnonic gain [103, 104]. These demonstrations confirm the experimental feasibility and practical relevance of the gain mechanism incorporated in our model.

ACKNOWLEDGEMENT

We acknowledge the financial support from the NSFC under grant No. 12174346.

REFERENCES

- [1] A. A. Serga, A. V. Chumak, and B. Hillebrands, Yig magnonics, *J. Phys. D: Appl. Phys.* **43**, 264002 (2010).
- [2] B. Lenk, H. Ulrichs, F. Garbs, and M. Münzenberg, The building blocks of magnonics, *Phys. Rep.* **507**, 107 (2011).
- [3] Z.-X. Liu, C. You, B. Wang, H. Xiong, and Y. Wu, Phase-mediated magnon chaos-order transition in cavity optomagnonics, *Opt. Lett.* **44**, 507 (2019).
- [4] C. Kong, H. Xiong, and Y. Wu, Magnon-induced nonreciprocity based on the magnon Kerr effect, *Phys. Rev. Appl.* **12**, 034001 (2019).
- [5] X. Zuo, Z.-Y. Fan, H. Qian, M.-S. Ding, H. Tan, H. Xiong, and J. Li, Cavity magnomechanics: from classical to quantum, *New J. Phys.* **26**, 031201 (2024).
- [6] Y.-P. Wang, G.-Q. Zhang, D. Zhang, X.-Q. Luo, W. Xiong, S.-P. Wang, T.-F. Li, C.-M. Hu, and J. Q. You, Magnon Kerr effect in a strongly coupled cavity-magnon system, *Phys. Rev. B* **94**, 224410 (2016).
- [7] P. Hyde, B. M. Yao, Y. S. Gui, G.-Q. Zhang, J. Q. You, and C.-M. Hu, Direct measurement of foldover in cavity magnon-polariton systems, *Phys. Rev. B* **98**, 174423 (2018).
- [8] Y. Cao, P. Yan, H. Huebl, S. T. B. Goennenwein, and G. E. W. Bauer, Exchange magnon-polaritons in mi-
- [9] B. M. Yao, Y. S. Gui, Y. Xiao, H. Guo, X. S. Chen, W. Lu, C. L. Chien, and C.-M. Hu, Theory and experiment on cavity magnon-polariton in the one-dimensional configuration, *Phys. Rev. B* **92**, 184407 (2015).
- [10] W.-L. Xu, Y.-P. Gao, T.-J. Wang, and C. Wang, Magnon-induced optical high-order sideband generation in hybrid atom-cavity optomagnonical system, *Opt. Express* **28**, 22334 (2020).
- [11] M. Yu, H. Shen, and J. Li, Magnetostrictively induced stationary entanglement between two microwave fields, *Phys. Rev. Lett.* **124**, 213604 (2020).
- [12] W. Qiu, X. Cheng, A. Chen, Y. Lan, and W. Nie, Controlling quantum coherence and entanglement in cavity magnomechanical systems, *Phys. Rev. A* **105**, 063718 (2022).
- [13] J. Li, S.-Y. Zhu, and G. S. Agarwal, Squeezed states of magnons and phonons in cavity magnomechanics, *Phys. Rev. A* **99**, 021801 (2019).
- [14] J. Li, Y.-P. Wang, J.-Q. You, and S.-Y. Zhu, Squeezing microwaves by magnetostriction, *Natl. Sci. Rev.* **10**, nwac247 (2022).

[15] H. Xiong, Controllable switching of the magnonic excitation based on the magnetostrictive effect, *Appl. Phys. Lett.* **124**, 112403 (2024).

[16] X. Zhang, C.-L. Zou, N. Zhu, F. Marquardt, L. Jiang, and H. X. Tang, Magnon dark modes and gradient memory, *Nat. Commun.* **6**, 8914 (2015).

[17] M. Harder, L. Bai, P. Hyde, and C.-M. Hu, Topological properties of a coupled spin-photon system induced by damping, *Phys. Rev. B* **95**, 214411 (2017).

[18] F. Wen, B. Guo, Y. Geng, F. Yang, and B. Wu, Tunable slow and fast light in a magneto-optic micro-ring resonator, *Appl. Phys. Express* **12**, 072011 (2019).

[19] B. Wang, Z.-X. Liu, C. Kong, H. Xiong, and Y. Wu, Magnon-induced transparency and amplification in pt-symmetric cavity-magnon system, *Opt. Express* **26**, 20248 (2018).

[20] K. Ullah, M. T. Naseem, and O. E. Müstecaplıoğlu, Tunable multiwindow magnomechanically induced transparency, Fano resonances, and slow-to-fast light conversion, *Phys. Rev. A* **102**, 033721 (2020).

[21] X. Li, W. X. Yang, T. Shui, L. Li, X. Wang, and Z. Wu, Phase control of the transmission in cavity magnomechanical system with magnon driving, *J. Appl. Phys.* **128**, 235101 (2020).

[22] T.-X. Lu, H. Zhang, Q. Zhang, and H. Jing, Exceptional-point-engineered cavity magnomechanics, *Phys. Rev. A* **103**, 063708 (2021).

[23] A. Munir, M. Abbas, Ziauddin, W.-M. Liu, and P. Zhang, Controllable magnon-induced transparency in a ferromagnetic material via cross- and self-Kerr effects, *J. Opt. Soc. Am. B* **40**, 1756 (2023).

[24] B. P. Hou, L. F. Wei, and S. J. Wang, Optomechanically induced transparency and absorption in hybridized optomechanical systems, *Phys. Rev. A* **92**, 033829 (2015).

[25] G. S. Agarwal and S. Huang, Electromagnetically induced transparency in mechanical effects of light, *Phys. Rev. A* **81**, 041803 (2010).

[26] X. Y. Zhang, Y. Q. Guo, P. Pei, and X. X. Yi, Optomechanically induced absorption in parity-time-symmetric optomechanical systems, *Phys. Rev. A* **95**, 063825 (2017).

[27] Z.-X. Liu, H. Xiong, and Y. Wu, Room-temperature slow light in a coupled cavity magnon-photon system, *IEEE Access* **7**, 57047 (2019).

[28] S.-N. Huai, Y.-L. Liu, J. Zhang, L. Yang, and Y.-x. Liu, Enhanced sideband responses in a \mathcal{PT} -symmetric-like cavity magnomechanical system, *Phys. Rev. A* **99**, 043803 (2019).

[29] U. Weiss, *Quantum Dissipative Systems*, 4th ed. (World Scientific, Singapore, 2012).

[30] S. K. Özdemir, S. Rotter, F. Nori, and L. Yang, Parity-time symmetry and exceptional points in photonics, *Nat. Mater.* **18**, 783 (2019).

[31] F. Minganti, A. Miranowicz, R. W. Chhajlany, and F. Nori, Quantum exceptional points of non-hermitian hamiltonians and liouvillians: The effects of quantum jumps, *Phys. Rev. A* **100**, 062131 (2019).

[32] A. Mostafazadeh, Pseudo-hermiticity versus pt symmetry: The necessary condition for the reality of the spectrum of a non-hermitian hamiltonian, *J. Math. Phys.* **43**, 205 (2002).

[33] A. Mostafazadeh, Pseudo-hermiticity versus pt-symmetry. ii. a complete characterization of non-hermitian hamiltonians with a real spectrum, *J. Math. Phys.* **43**, 2814 (2002).

[34] V. V. Konotop, J. Yang, and D. A. Zezyulin, Nonlinear waves in \mathcal{PT} -symmetric systems, *Rev. Mod. Phys.* **88**, 035002 (2016).

[35] W. Xiong, Z. Li, Y. Song, J. Chen, G.-Q. Zhang, and M. Wang, Higher-order exceptional point in a pseudo-Hermitian cavity optomechanical system, *Phys. Rev. A* **104**, 063508 (2021).

[36] G. Zhang, S. Lin, W. Feng, Y. Wang, Y. Yu, and C. Yang, Third-order exceptional surface in a pseudo-hermitian superconducting circuit, *Sci. China Inf. Sci.* **68**, 180508 (2025).

[37] C. M. Bender, B. K. Berntson, D. Parker, and E. Samuel, Observation of pt phase transition in a simple mechanical system, *Am. J. Phys.* **81**, 173 (2013).

[38] Y.-L. Liu, R. Wu, J. Zhang, S. K. Özdemir, L. Yang, F. Nori, and Y.-x. Liu, Controllable optical response by modifying the gain and loss of a mechanical resonator and cavity mode in an optomechanical system, *Phys. Rev. A* **95**, 013843 (2017).

[39] P. Midya, Y. G. N. Liu, B. Bahari, M. Khajavikhan, and D. N. Christodoulides, Non-hermitian and topological photonics: optics at an exceptional point, *Nanophotonics* **10**, 403 (2021).

[40] H. Jing, S. K. Özdemir, X.-Y. Lü, J. Zhang, L. Yang, and F. Nori, \mathcal{PT} -symmetric phonon laser, *Phys. Rev. Lett.* **113**, 053604 (2014).

[41] H. Xu, D. Mason, L. Jiang, and J. G. E. Harris, Topological energy transfer in an optomechanical system with exceptional points, *Nature* **537**, 80 (2016).

[42] J. Doppler, A. A. Mailybaev, J. Böhm, U. Kuhl, A. Girschik, F. Libisch, T. J. Milburn, P. Rabl, N. Moiseyev, and S. Rotter, Dynamically encircling an exceptional point for asymmetric mode switching, *Nature* **537**, 76 (2016).

[43] L. Chang, X. Jiang, S. Hua, C. Yang, J. Wen, L. Jiang, G. Li, G. Wang, and M. Xiao, Parity-time symmetry and variable optical isolation in active-passive-coupled microresonators, *Nat. Photonics* **8**, 524 (2014).

[44] D. Zhang, X.-Q. Luo, Y.-P. Wang, T.-F. Li, and J. Q. You, Observation of the exceptional point in cavity magnon-polaritons, *Nat. Commun.* **8**, 1368 (2017).

[45] W. D. Heiss and G. Wunner, A model of three coupled wave guides and third order exceptional points, *J. Phys. A* **49**, 495303 (2016).

[46] G.-Q. Zhang and J. Q. You, Higher-order exceptional point in a cavity magnonics system, *Phys. Rev. B* **99**, 054404 (2019).

[47] G. Demange and E.-M. Graefe, Signatures of three coalescing eigenfunctions, *J. Phys. A* **45**, 025303 (2011).

[48] W. D. Heiss, Chirality of wavefunctions for three coalescing levels, *J. Phys. A* **41**, 244010 (2008).

[49] H. Hodaei, A. U. Hassan, S. Wittek, H. Garcia-Gracia, R. El-Ganainy, D. N. Christodoulides, and M. Khajavikhan, Enhanced sensitivity at higher-order exceptional points, *Nature* **548**, 187 (2017).

[50] C. Zeng, K. Zhu, Y. Sun, G. Li, Z. Guo, J. Jiang, Y. Li, H. Jiang, Y. Yang, and H. Chen, Ultra-sensitive passive wireless sensor exploiting high-order exceptional point for weakly coupling detection, *New J. Phys.* **23**, 063008 (2021).

[51] K. Ding, G. Ma, M. Xiao, Z. Q. Zhang, and C. T. Chan, Emergence, coalescence, and topological properties of multiple exceptional points and their experimental realization, *Phys. Rev. X* **6**, 021007 (2016).

[52] P. Delplace, T. Yoshida, and Y. Hatsugai, Symmetry-protected multifold exceptional points and their topological characterization, *Phys. Rev. Lett.* **127**, 186602 (2021).

[53] Z. Lin, A. Pick, M. Lončar, and A. W. Rodriguez, Enhanced spontaneous emission at third-order dirac exceptional points in inverse-designed photonic crystals, *Phys. Rev. Lett.* **117**, 107402 (2016).

[54] S. Das, S. Chakraborty, and T. N. Dey, Gain-assisted controllable fast-light generation in cavity magnomechanics, *Phys. Rev. A* **108**, 033517 (2023).

[55] F. Wang and C. Gou, Magnon-induced absorption via quantum interference, *Opt. Lett.* **48**, 1164 (2023).

[56] S. Bayati, M. B. Harouni, and A. Mahdifar, Magnomechanically induced transparency and tunable slow-fast light via a levitated micromagnet, *Opt. Express* **32**, 14914 (2024).

[57] A. Wahab, M. Abbas, X. Yang, and Y. Chen, Tunable optical amplification and group delay in cavity magnomechanics, *Eur. Phys. J. Plus* **140**, 44 (2025).

[58] M. Onoda, S. Murakami, and N. Nagaosa, Hall effect of light, *Phys. Rev. Lett.* **93**, 083901 (2004).

[59] M. Kim, Y. Yang, D. Lee, Y. Kim, H. Kim, and J. Rho, Spin Hall effect of light: from fundamentals to recent advancements, *Laser Photonics Rev.* **17**, 2200046 (2023).

[60] K. Y. Bliokh and Y. P. Bliokh, Conservation of angular momentum, transverse shift, and spin Hall effect in reflection and refraction of an electromagnetic wave packet, *Phys. Rev. Lett.* **96**, 073903 (2006).

[61] O. Hosten and P. Kwiat, Observation of the spin Hall effect of light via weak measurements, *Science* **319**, 787 (2008).

[62] C. Imbert, Calculation and experimental proof of the transverse shift induced by total internal reflection of a circularly polarized light beam, *Phys. Rev. D* **5**, 787 (1972).

[63] F. I. Fedorov, To the theory of total reflection*, *J. Opt.* **15**, 014002 (2013).

[64] X. Yin, Z. Ye, J. Rho, Y. Wang, and X. Zhang, Photonic spin Hall effect at metasurfaces, *Science* **339**, 1405 (2013).

[65] M. Shah and M. Sajid, Surface states-dependent giant quantized photonic spin Hall effect in a magnetic topological insulator thin film, *Phys. E* **138**, 115113 (2022).

[66] X. Zhou, X. Ling, H. Luo, and S. Wen, Identifying graphene layers via spin Hall effect of light, *Appl. Phys. Lett.* **101**, 251602 (2012).

[67] M. Shah, M. Shah, N. A. Khan, M. Sajid, M. Jan, and G. Xianlong, Tunable quantized spin Hall effect of light in graphene, *Results Phys.* **60**, 107676 (2024).

[68] L. Cai, M. Liu, S. Chen, Y. Liu, W. Shu, H. Luo, and S. Wen, Quantized photonic spin Hall effect in graphene, *Phys. Rev. A* **95**, 013809 (2017).

[69] W. J. M. Kort-Kamp, Topological phase transitions in the photonic spin Hall effect, *Phys. Rev. Lett.* **119**, 147401 (2017).

[70] M. Shah, Probing topological quantum phase transitions via photonic spin Hall effects in spin-orbit coupled 2D quantum materials, *J. Phys. D: Appl. Phys.* **55**, 105105 (2021).

[71] L. Salasnich, Enhancement of four reflection shifts by a three-layer surface-plasmon resonance, *Phys. Rev. A* **86**, 055801 (2012).

[72] X. Zhou and X. Ling, Enhanced photonic spin Hall effect due to surface plasmon resonance, *IEEE Photonics J.* **8**, 1 (2016).

[73] X.-J. Tan and X.-S. Zhu, Enhancing photonic spin Hall effect via long-range surface plasmon resonance, *Opt. Lett.* **41**, 2478 (2016).

[74] P. Gosselin, A. Bérard, and H. Mohrbach, Spin Hall effect of photons in a static gravitational field, *Phys. Rev. D* **75**, 084035 (2007).

[75] J.-M. Ménard, A. E. Mattacchione, M. Betz, and H. M. van Driel, Imaging the spin Hall effect of light inside semiconductors via absorption, *Opt. Lett.* **34**, 2312 (2009).

[76] M. Abbas, G. Din, H. R. Hamed, and P. Zhang, Manipulation of the photonic spin Hall effect in a cavity magnomechanical system, *Phys. Rev. A* **111**, 053716 (2025).

[77] A. Munir, M. Abbas, Ziauddin, and C. Wang, Coherent- and dissipative-coupling control of photonic spin Hall effect in cavity magnomechanical system, *Opt. Laser Technol.* **188**, 112813 (2025).

[78] X. Zhou, X. Lin, Z. Xiao, T. Low, A. Alù, B. Zhang, and H. Sun, Controlling photonic spin Hall effect via exceptional points, *Phys. Rev. B* **100**, 115429 (2019).

[79] M. Ullah, A. Abbas, J. Jing, and L.-G. Wang, Flexible manipulation of the Goos-Hänchen shift in a cavity optomechanical system, *Phys. Rev. A* **100**, 063833 (2019).

[80] L.-G. Wang, M. Ikram, and M. S. Zubairy, Control of the Goos-Hänchen shift of a light beam via a coherent driving field, *Phys. Rev. A* **77**, 023811 (2008).

[81] N. Pramanik, K. C. Yellapragada, S. Singh, and P. A. Lakshmi, Coherent control of Fano resonances in a macroscopic four-mirror cavity, *Phys. Rev. A* **101**, 043802 (2020).

[82] W. Ge, M. Al-Amri, H. Nha, and M. S. Zubairy, Entanglement of movable mirrors in a correlated emission laser via cascade-driven coherence, *Phys. Rev. A* **88**, 052301 (2013).

[83] B. Teklu, T. Byrnes, and F. S. Khan, Cavity-induced mirror-mirror entanglement in a single-atom Raman laser, *Phys. Rev. A* **97**, 023829 (2018).

[84] J. Li, S.-Y. Zhu, and G. S. Agarwal, Magnon-phonon-phonon entanglement in cavity magnomechanics, *Phys. Rev. Lett.* **121**, 203601 (2018).

[85] W. Li, Y. Jiang, C. Li, and H. Song, Parity-time-symmetry enhanced optomechanically-induced-transparency, *Sci. Rep.* **6**, 31095 (2016).

[86] M. Waseem, M. Irfan, and S. Qamar, Magnomechanically controlled Goos-Hänchen shift in cavity QED, *Phys. Rev. A* **110**, 033711 (2024).

[87] H. Xiong, L. Si, X. Lv, X. Yang, and Y. Wu, Review of cavity optomechanics in the weak-coupling regime: from linearization to intrinsic nonlinear interactions, *Sci. China Phys. Mech. Astron.* **58**, 1 (2015).

[88] Y. He and Q. Chen, Sensitivity of mass sensors enhanced by higher-order exceptional points in an optomechanical system, *Laser Phys.* **34**, 055206 (2024).

[89] F. Chen, Electromagnetically induced grating in a nonlinear optomechanical cavity, *Laser Phys. Lett.* **20**, 095206 (2023).

[90] L. Li, W. Nie, and A. Chen, Transparency and tunable slow and fast light in a nonlinear optomechanical cavity,

Sci. Rep. **6**, 35090 (2016).

[91] D. F. Walls and G. J. Milburn, *Quantum Optics* (Springer-Verlag, Berlin, Heidelberg, 1994).

[92] K. Y. Bliokh, F. J. Rodríguez-Fortuño, F. Nori, and A. V. Zayats, Spin-orbit interactions of light, *Nat. Photonics* **9**, 796 (2015).

[93] S. Asiri, J. Xu, M. Al-Amri, and M. S. Zubairy, Controlling the Goos-Hänchen and Imbert-Fedorov shifts via pump and driving fields, *Phys. Rev. A* **93**, 013821 (2016).

[94] Y. Xiang, X. Jiang, Q. You, J. Guo, and X. Dai, Enhanced spin Hall effect of reflected light with guided-wave surface plasmon resonance, *Photon. Res.* **5**, 467 (2017).

[95] K. Y. Bliokh and Y. P. Bliokh, Polarization, transverse shifts, and angular momentum conservation laws in partial reflection and refraction of an electromagnetic wave packet, *Phys. Rev. E* **75**, 066609 (2007).

[96] H. Luo, X. Zhou, W. Shu, S. Wen, and D. Fan, Enhanced and switchable spin Hall effect of light near the Brewster angle on reflection, *Phys. Rev. A* **84**, 043806 (2011).

[97] X. Zhang, C.-L. Zou, L. Jiang, and H. X. Tang, Cavity magnomechanics, *Sci. Adv.* **2**, e1501286 (2016).

[98] C. E. Rüter, K. G. Makris, R. El-Ganainy, D. N. Christodoulides, M. Segev, and D. Kip, Observation of parity-time symmetry in optics, *Nat. Phys.* **6**, 192 (2010).

[99] M. Waseem, M. Shah, and G. Xianlong, Gain-assisted control of the photonic spin Hall effect, *Phys. Rev. A* **110**, 033104 (2024).

[100] T. Brächer, P. Pirro, and B. Hillebrands, Parallel pumping for magnon spintronics: Amplification and manipulation of magnon spin currents on the micron-scale, *Phys. Rep.* **699**, 1 (2017).

[101] S. O. Demokritov, V. E. Demidov, O. Dzyapko, G. A. Melkov, A. A. Serga, B. Hillebrands, and A. N. Slavin, Bose-Einstein condensation of quasi-equilibrium magnons at room temperature under pumping, *Nature* **443**, 430 (2006).

[102] B. Heinz, M. Mohseni, A. Lentfert, R. Verba, M. Schneider, B. Lägel, K. Levchenko, T. Brächer, C. Dubs, A. V. Chumak, and P. Pirro, Parametric generation of spin waves in nanoscaled magnonic conduits, *Phys. Rev. B* **105**, 144424 (2022).

[103] J. W. Rao, B. Yao, C. Y. Wang, C. Zhang, T. Yu, and W. Lu, Unveiling a pump-induced magnon mode via its strong interaction with walker modes, *Phys. Rev. Lett.* **130**, 046705 (2023).

[104] Z. Chen, J. Rao, K. X. Zhao, F. Yang, C. X. Wang, B. Yao, and W. Lu, Manipulating the nonreciprocal microwave transmission by using a pump-induced magnon mode, *Appl. Phys. Lett.* **125**, 042403 (2024).